Research Article | Vol. 33, No. 12 / 16 Jun 2025 / Optics Express 24292
Optics EXPRESS

Angle tunable frequency conversion in form-birefringent nonlinear metamaterials

MAI TAL[1,2,3,*] AND TAL ELLENBOGEN[2,3]

[1]School of Physics and Astronomy, Tel-Aviv University, Tel-Aviv 6779801, Israel
[2]Department of Physical Electronics, Faculty of Engineering, Tel-Aviv University, Tel-Aviv 6779801, Israel
[3]Center for Light-Matter Interaction, Tel-Aviv University, Tel-Aviv 6779801, Israel
[*]maital@mail.tau.ac.il

Abstract: Phase matching (PM) of nonlinear optical interactions is central for obtaining efficient frequency conversion. Birefringent PM, which is highly useful in anisotropic nonlinear crystals, is limited by intrinsic bulk properties. However, application of this method can extend beyond natural constraints through form-birefringence in layered metamaterials. Here, we theoretically and numerically analyze angle-tuned form-birefringent PM in an infinite periodic laminar metamaterial, consisting of GaAs and SiN. We demonstrate configurations for efficient second harmonic generation of near-infrared radiation and difference-frequency-generation of mid-infrared light. An angular tunability of over an octave for mid-infrared generation in the range of $\sim 3.3-6.7\ \mu m$ is demonstrated. These findings motivate the construction of bulk form-birefringent metamaterials as a new platform for nonlinear optics.

1. Introduction

Generation of light by frequency conversion in nonlinear crystals is implemented in a wide range of coherent optical sources, from simple compact lasers, through advanced commercial optical parametric oscillators [1,2], to novel quantum light emitters [3,4]. The frequency conversion efficiency for interacting waves that propagate in a nonlinear medium, strongly depends on their relative accumulated phase. To achieve a coherent buildup of the nonlinear signal, leading to efficient conversion, phase matching (PM) of the waves is required [5]. However, due to the natural dispersion of bulk nonlinear crystals, PM between waves of different frequencies is not trivially fulfilled. Therefore, different methods are employed in various systems to attain PM.

A few prominent examples for PM methods are: modal PM in waveguide systems, which exploits the influence of the waveguide geometry on the propagation constants of the guided modes [6,7], quasi-PM in periodically-poled crystals, which relies on a spatial modulation of the nonlinear response [2,8], and birefringent PM (BPM) in uniaxial or biaxial crystals, which phase-matches processes involving interacting waves of orthogonal polarizations [9,10]. In BPM the PM condition is exactly satisfied using the intrinsic anisotropy of the nonlinear crystal. Moreover, it can be tuned by varying the angle of propagation relative to the crystal axes. Yet, throughout the variety of PM techniques, there are generally inherent compromises enforced between desired attributes, such as broad material compatibility, tunability, and flexibility in determining the physical dimensions of the system.

A promising engineered-material approach to allow PM in a wide range of materials and geometries, is based on nonlinear laminar composites with a subwavelength periodic refractive index profile [11]. First, it is possible to use these structures by harnessing the strong dispersion near photonic crystal modes. This has been done extensively in Bragg configuration [12], which entails working near the stop bands of the system. It has also been demonstrated in Laue configuration, yielding tunable phase matched transmitted and diffracted harmonic generation [13]. Another approach suggests using the unique dispersion properties of hybrid dielectric-metallic composites [14]. Yet the presence of metallic layers in these structures introduces

#558436 https://doi.org/10.1364/OE.558436
Journal © 2025 Received 29 Jan 2025; revised 27 Apr 2025; accepted 1 May 2025; published 2 Jun 2025

Optics EXPRESS

losses which limit the propagation lengths. A third method which does not require the vicinity of the stop band, can act only on the zero order transmitted light and can be implemented in all-dielectric systems, aims to harness the different boundary conditions imposed on TE and TM polarized light propagating parallel to the layers of the composite [15,16]. The distinct boundary conditions lead to a structural anisotropy, called form-birefringence, which does not rely on the microscopic composition of the layers.

Form-birefringence is a well-studied phenomenon in linear optics, with diverse applications ranging from commonly used wire-grid polarizers [17] to implementations in optical metasurfaces [18–20], optomechanical control [21,22] and integrated optical devices [23]. In nonlinear optics, form-birefringence can be used to augment the natural anisotropy of a nonlinear crystal for the purpose of BPM in a frequency conversion process. Remarkably, it can be applied to isotropic nonlinear crystals, which completely forbid this practice when in their bulk form [16]. Such crystals may have large nonlinear coefficients, as well as other attractive properties for frequency conversion applications, making the prospect of incorporating them into phase-matched elements highly appealing [24]. Indeed, experimental realizations of form-birefringent PM (FBPM) were studied in waveguides composed of GaAs and oxidized AlGaAs layers, both intrinsically isotropic [24–27]. However, although FBPM was initially suggested as a bulk media platform [16], so far only a few works have addressed FBPM in bulk systems [16,28,29].

In recent years, research on bulk and multilayered optical metamaterials has expanded rapidly [29–35], driven by advances in fabrication techniques [30,31,34,35] as well as theoretical and computational methods [30,32,33]. Exploiting FBPM to engineer nonlinear nanostructured bulk metamaterials, with designed phase relations between the interacting waves, may allow an exceptional control over the nonlinear light-matter interaction in three-dimensional structures.

In this paper we study FBPM in a bulk laminar nonlinear metamaterial and reveal some of its promising attributes. We use an overlap analysis to estimate the effective composite nonlinear coefficient. Furthermore, we analyze the case of off-axis propagation of the interacting waves and apply it to PM of second harmonic generation (SHG) and difference frequency generation (DFG). By addressing this degree of freedom, so far overlooked in the study of FBPM, we show that an octave-spanning tunability of DFG for generation of mid-IR radiation can be achieved in a GaAs-SiN composite. This makes the proposed metamaterial an artificial analogue of the widespread uniaxial crystals, but with rigorously adjustable properties, extending the selection of materials available for frequency conversion, and opening the door for enhanced control of light propagation in nonlinear media.

2. Theoretical background

The system under study is illustrated in Fig. 1(A). The metamaterial is composed of an infinite subwavelength laminar structure with alternating layers of two materials 1 and 2, with thicknesses d_1 and d_2 and refractive indices n_1 and n_2. Material 1 is a linear material and material 2 is a quadratic nonlinear material that supports three-wave-mixing interactions. Along the $\hat{z}$ and $\hat{x}$ directions there is continuous translation symmetry and in the $\hat{y}$ direction there is a discrete symmetry to translations of $m\Lambda = m(d_1 + d_2)$ where m is an integer. The origin of form-birefringence is illustrated in Fig. 1(B), where the electric field distribution of the two orthogonal polarizations, for waves moving parallel to the layer interfaces, is shown. The electric field of transverse electric (TE) polarized light obeys continuity at the boundaries, leading to a smooth field distribution. Conversely, the $\hat{y}$ component of the electric field of transverse magnetic (TM) polarized light experiences a jump at layer interfaces. This results in a tendency of TM waves to be localized in the low-index medium, which we select to be material 1.

For deep subwavelength layers, a straightforward effective medium calculation can be performed [36] which shows an equivalence between the laminar metamaterial and a negative uniaxial crystal. The isofrequency curves of the metamaterial for light propagating in the $y-z$ plane are

Optics EXPRESS

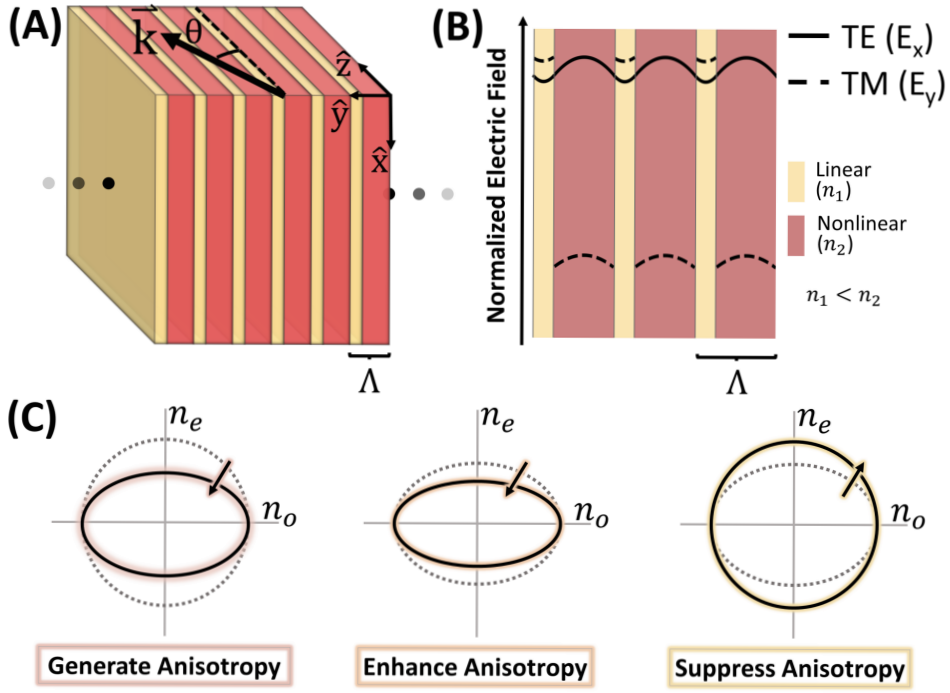

Fig. 1. (A) The nonlinear metamaterial, composed of a nonlinear crystal (red) and a linear refractive index contrast material (yellow) in a subwavelength laminar structure. (B) Normalized electric field distribution for TE (smooth line) and TM (dashed line) waves for propagation along the $\hat{z}$ direction ($\theta = 0^\circ$) with $n_1 < n_2$. The different boundary conditions for TE and TM waves lead to different field distributions, resulting in form-birefringence. (C) Form-birefringence augmentation of the polarization ellipse. Dotted lines illustrate the intrinsic properties of the nonlinear film, solid lines are the normalized transformation created by the laminar structure. Three cases are illustrated: when using fully isotropic layers anisotropy can be generated (left), a naturally birefringent material's anisotropy can be enhanced (middle) or even fully suppressed (right).

expressed through the following set of equations

$$\begin{aligned} &\textbf{TE} \\ &\frac{K^2}{\tilde{n}_o^2} + \frac{\beta^2}{\tilde{n}_o^2} = \left(\frac{\omega}{c_0}\right)^2 \\ &\textbf{TM} \\ &\frac{K^2}{\tilde{n}_o^2} + \frac{\beta^2}{\tilde{n}_e^2} = \left(\frac{\omega}{c_0}\right)^2 \end{aligned} \tag{1}$$

where ω is the light's frequency and c_0 the speed of light in vacuum. β and K define the wave vector in the metamaterial $\mathbf{k} = K\hat{y} + \beta\hat{z}$. The effective indices in this case are given by [36]

$$\begin{aligned} \tilde{n}_o^2 &= \frac{d_1}{\Lambda} n_1^2 + \left(1 - \frac{d_1}{\Lambda}\right) n_2^2 \\ \frac{1}{\tilde{n}_e^2} &= \frac{d_1}{\Lambda} \frac{1}{n_1^2} + \left(1 - \frac{d_1}{\Lambda}\right) \frac{1}{n_2^2} \end{aligned} \tag{2}$$

and depend solely on n_1, n_2 and on the ratio d_1/Λ. This provides a means to tune the polarization ellipse of the artificial material.

Optics EXPRESS

Figure 1(C) shows three examples of possible augmentations to the intrinsic polarization ellipse of a nonlinear crystal, as described by Eqs. (1) and (2). First, when both materials 1 and 2 are non-birefringent materials, form-birefringence allows the generation of anisotropy. Furthermore, allowing the nonlinear material 2 to support birefringence, specific orientations of the crystal axes relative to the periodicity can enhance or counteract its natural birefringence.

In general, form-birefringence remains present in the system also if the period is not deeply-subwavelength. However, in this case the simple model of Eqs. (1) no longer holds, and special care needs to be taken in order to calculate the constants of propagation [11,36]. For a given frequency ω, the relationship between β and K can be found by numerically solving the following dispersion relation [37]

$$\begin{aligned}\cos(K\Lambda) = &\cos\left(k_{1y}d_1\right)\cos\left(k_{2y}d_2\right)\\ -\tfrac{1}{2}&\left(p^2\frac{k_{1y}}{k_{2y}}+\frac{1}{p^2}\frac{k_{2y}}{k_{1y}}\right)\sin\left(k_{1y}d_1\right)\sin\left(k_{2y}d_2\right)\end{aligned} \tag{3}$$

where $k_{iy} = \sqrt{\left(\frac{n_i\omega}{c_0}\right)^2 - \beta^2}$ and p is a factor which differs for TE ($p = 1$) and TM ($p = n_2/n_1$) polarizations. For parameters of the system such that the Bragg diffraction condition is approached, reflection and diffraction effects need to be considered and a dynamical diffraction formulation is required [13]. In this paper, however, we limited our calculations so that all frequency components participating in the nonlinear interaction remain inside the first photonic band of the structure, and away from the lowest frequency band-gap edge.

Within these boundaries Eq. (3) yields real $\mathbf{k}$ values, corresponding to propagating waves. From the calculated pair β, K, the effective index and propagation angle can be extracted using [11]

$$n_{eff} = \frac{c_0}{\omega}\sqrt{\beta^2 + K^2} \quad ; \quad \theta = \arctan\left(\frac{K}{\beta}\right) \tag{4}$$

In contrast to the case of very thin layers (Eqs. (1)), the isofrequency curves calculated within this framework are not necessarily elliptical, and the effective indices may explicitly depend on the thicknesses d_1 and d_2 [36].

The infinite nature of the system described here provides an approximation for real physical devices. It has been previously shown that the set of effective indices calculated using this framework serves as a helpful starting point, even when analyzing form-birefringent devices with only a few layers [24,28].

3. Results

To allow for quantitative assessment of the potential of FBPM in bulk metamaterials, we examined a combination of GaAs for the nonlinear material and SiN as the contrast layer. GaAs was chosen for its exceptionally strong nonlinearity ($d_{36} \sim 100$ pm/V) [38], which makes it highly attractive for frequency conversion applications. In addition, GaAs has an isotropic structure, which forbids the use of BPM in its natural form. SiN was selected to provide a balance between several considerations, namely, fabrication compatibility [39], overlap in the transparency band [40,41], and a refractive index which differs from that of GaAs by ~ 1. The latter is useful in obtaining a laminar structure with a large refractive index contrast, to attain strong form-anisotropy which supports FBPM of a wide range of frequency mixing processes [16].

3.1. Second harmonic generation

We began with an analysis of FBPM of SHG. We assumed that the GaAs films are oriented so that the GaAs [001] direction points towards the metamaterial's $\hat{y}$ axis (see Fig. 1(A)). This way, a TE pump wave polarized along the GaAs [110] direction can generate a TM polarized second

Optics EXPRESS

harmonic (SH), through the d_{36} nonlinear element [42]. For a fundamental frequency (FF) wave with a free-space wavelength λ_0, the momentum mismatch of such a process is

$$\Delta k = \frac{4\pi}{\lambda_0}\left(n^{TE}_{\lambda_0}(\theta) - n^{TM}_{\lambda_0/2}(\theta)\right) \tag{5}$$

where the effective indices $n^{TE}_{\lambda_0}(\theta)$ and $n^{TM}_{\lambda_0/2}(\theta)$ of the FF and SH respectively, are calculated using Eq. (4), and the PM condition dictates $\Delta k = 0$. The process described by Eq. (5) is the analogy of type I SHG in a negative uniaxial crystal, but here the magnitude of birefringence and its angular dependence can be controlled by selecting the layers thickness [11,16]. Figure 2(A) shows the momentum mismatch map for $d_{GaAs} = 120$ nm and $\theta = 0°$, for varying d_{SiN} values, where the existence of a tailored PM condition is evident. For example, selecting $d_{SiN} = 20$ nm, the PM condition is fulfilled near a fundamental wavelength of $\lambda_0 = 1.817\ \mu m$.

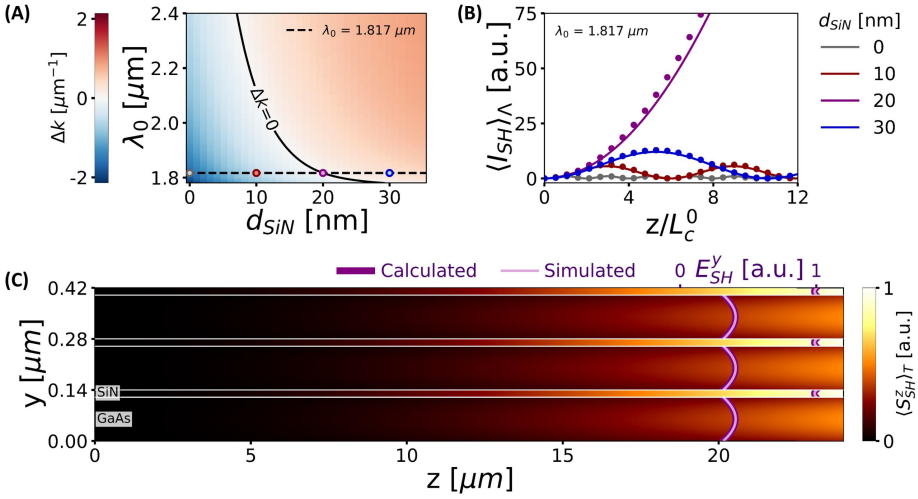

Fig. 2. SHG in a GaAs, SiN laminar structure for $\theta = 0°$. (A) Momentum mismatch for constant $d_{GaAs} = 120$ nm, as a function of d_{SiN} and λ_0. The FF is TE polarized, and the SH is TM polarized. The solid black line marks the PM curve. The dashed black line marks $\lambda_0 = 1.817\ \mu m$, for which the PM condition is fulfilled near $d_{SiN} = 20$ nm. Four coloured dots correspond to the curves in (B). (B) Calculated (lines) and simulated (dots) averaged SH intensity $\langle I_{SH}\rangle_\Lambda$ as function of propagation distance z. In bulk GaAs ($d_{SiN} = 0$) the SH signal oscillates with the typical coherence length L^0_C (Eq. (6)). Intensity values are normalized by the maximal bulk SH intensity. (C) Colormap - simulated SH time-averaged $\hat{z}$ component of the SH Poynting vector, $\langle S^z_{SH}\rangle_T$ associated with the purple dots in (B), in three replicas of the simulation unit cell. Overlaid lines on the right side of the plot, show the $\hat{y}$-polarized electric field, E^y_{SH} as analytically calculated for the TM mode at $\lambda_0/2$ (dark purple), and from the SH interface as extracted at the output of the simulation (light purple).

For these parameters, the value for the FF effective index calculated exactly from Eq. (4), differs only by 0.07% from that calculated with the uniaxial approximation in Eqs. (2). The SH effective index, however, is affected to a greater extent and differs by 1.78% from the uniaxial approximation. This leads to a substantial deviation between the exactly calculated and approximated Δk, emphasizing the need to use the exact formulation in this work.

Assuming a lossless medium, the nonlinear signal intensity at the PM condition is expected to grow quadratically with the propagation distance in the metamaterial. For a finite mismatch,

Optics EXPRESS

the nonlinear signal is bounded and oscillates along the propagation axis, obtaining its maximal values in odd multiples of the coherence length

$$L_C = \frac{\pi}{|\Delta k|} \tag{6}$$

For a more detailed description of the evolution of the SH signal under propagation through the metamaterial, we considered the effect of the layers on the nonlinear coupling, using a coupled-mode formalism [42,43]. We looked at the SH intensity averaged over a period Λ, and obtained

$$\langle I_{SH}\rangle_\Lambda(z) \propto \frac{\langle I_0\rangle_\Lambda^2}{n_{\lambda_0}^2 n_{\lambda_0/2}\lambda_0^2}\zeta^2 d^2 z^2 \mathrm{sinc}\left(\frac{\Delta k z}{2}\right)^2 \tag{7}$$

where $\langle I_0\rangle_\Lambda$ is the averaged pump intensity and d is the nonlinear tensor coefficient. For $\theta = 0°$ and under the orientation and polarization configuration described previously, $d = d_{36}$. ζ is an overlap integral function that describes the modification of the effective nonlinearity by the layered structure. We calculate ζ as

$$\zeta = \Lambda^{1/2}\frac{\int_{\Lambda,\chi^{(2)}} E^x_{\lambda_0}(y)^2 E^y_{\lambda_0/2}(y)dy}{\left[\int_\Lambda E^y_{\lambda_0/2}(y)^2 dy\right]^{1/2}\int_\Lambda E^x_{\lambda_0}(y)^2 dy} \tag{8}$$

where $E^x_{\lambda_0}(y)$ and $E^y_{\lambda_0/2}(y)$ are the field profiles of the $\hat{x}$ directed FF and the $\hat{y}$ directed SH, respectively, calculated using the framework of Eq. (3) [37]. The integration is to be performed over one period of the metamaterial, and the $\chi^{(2)}$ sign in the numerator indicates that this integration is done only in the nonlinear region. For simplicity of calculation, we neglected the $\hat{z}$ component of the TM polarized SH electric field.

Figure 2(B) shows $\langle I_{SH}\rangle_\Lambda$ as calculated from Eq. (7) for $\lambda_0 = 1.817\ \mu m$ and for several SiN thicknesses. It can be seen that in bulk GaAs ($d_{SiN} = 0$) the SH signal rapidly oscillates due to the intrinsic GaAs dispersion. For $d_{SiN} \neq 0$ the oscillation length-scale and amplitude changes according to the effective material properties, with a coherent buildup over many bulk coherence lengths at $d_{SiN} = 20$ near perfect PM.

To validate these results, we conducted simulations with the finite element method (FEM), performed in COMSOL [44]. The simulations used two electromagnetic waves, frequency domain interfaces, for the FF and the SH, coupled by polarization nodes. The simulations were conducted within one symmetric period of the structure in the $\hat{y}$ direction, with periodic y boundary conditions. In the FF physics interface one of the z boundaries included plane-wave excitation. From the simulations, the time-averaged $\hat{z}$ component of the SH Poynting vector, $\langle S^z_{SH}\rangle_T$, was extracted. Additionally, the SH field in the $\hat{y}$ direction E^y_{SH} was extracted at the output boundary of the simulation.

The dots in Fig. 2(B) mark the results extracted from the simulations. A good agreement can be observed between the simulation results and the prediction of Eq. (7). The slight deviation may stem from the simplified calculation of ζ in Eq. (8). Figure 2(C) shows the simulated spatial distribution of $\langle S^z_{SH}\rangle_T$, the time-averaged $\hat{z}$ component of the SH Poynting vector. In addition to the coherent buildup of the SH, the localization of the TM polarized SH signal in the low index SiN layer can be clearly observed. Figure 2(C) shows also the analytically calculated metamaterial TM mode profile at the SH wavelength [37], along with the SH field extracted at the output of the simulation, which are in perfect agreement.

To leverage the full capabilities of FBPM in the bulk layered metamaterial it is important to study PM at oblique incidence, as defined in Fig. 1(A). This degree of freedom can be used to significantly extend the usable PM frequency range of the metamaterial, as well as compensate for possible fabrication inaccuracies. To demonstrate it, we continued with the combination of

Optics EXPRESS

d_{GaAs} = 120 nm and d_{SiN} = 20 nm, but now selected a pump wavelength of $\lambda_0 = 2\ \mu m$, where the SHG is not phase matched for $\theta = 0°$ (see Fig. 2(A)). By tuning the propagation angle, PM of this interaction can be attained, leading to efficient SHG as shown in Fig. 3(A). The top part shows the propagation angle dependent effective refractive indices of the FF and SH waves, in accordance with Eq. (5). It can be seen that the effective refractive index of the TM mode has high angular dispersion, while that of the TE mode is fixed, as expected. Near an angle of $\theta = 37°$ the curves intersect and the PM condition is fulfilled, as is apparent from the coherence length plotted in Fig. 3(B) which peaks at the intersection. Figure 3(A),(B) also show the predictions of the uniaxial approximation (Eq. (1)). Even though with the selected parameters the structural dispersion is not negligible, the PM angle is shifted only by a few degrees from the deep subwavelength case. Due to the high effective index (n ~ 3.2), excitation from free-space for a facet that is normal to the layers is prohibited for this angle. This can be overcome, for example, by using a technique such as prism coupling, or by cutting the device at an angle to the planes of the laminar structure in a manner similar to conventional nonlinear crystals.

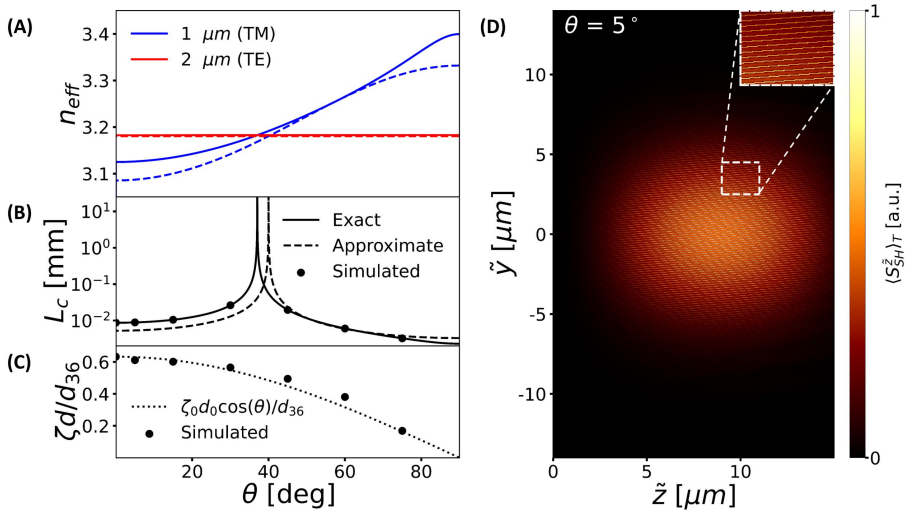

Fig. 3. Angle tuned SHG in a GaAs, SiN laminar structure. (A) Angle dependent effective refractive indices for $\lambda_0 = 2\ \mu m$, calculated using Eq. (4) (Solid lines). The indices are equal near 37°. Dashed lines show the indices calculated using the uniaxial approximation (Eq. (2)). (B) Coherence lengths, L_C, extracted from the effective index values and peak at the PM angle. Black dots indicate L_c extracted from FEM simulations. (C) Composite nonlinear coefficient, ζd, as function of propagation angle. Dots represent the values obtained from FEM simulations, normalized by the d_{36} element of GaAs. The dotted line corresponds to an angular dependence influenced only by the polarization relative to the GaAs crystal axes. $\zeta_0 d_0$ is the value at 0°. (D) An example of the time-averaged Poynting vector along the pump propagation direction $\langle S^{\tilde{z}}_{SH} \rangle_T$, for the SH beam generated at $\theta = 5°$, oscillating due to the phase mismatch. The axes $\tilde{y}, \tilde{z}$ are rotated by an angle θ relative to $\hat{y}, \hat{z}$ defined in Fig. 1(A).

Figure 3(B) includes coherence length values extracted by fitting simulation data to Eq. (7), showing an excellent agreement with the values calculated using Eq. (4). FEM simulations were conducted following the manner described previously. However, instead of a single periodic domain, the simulation region was set up as depicted in Fig. 3(D). FF excitation was injected as a Gaussian beam with a full waist of $2w_0 = 20\ \mu m$. The simulation domain consisted of alternating GaAs layers and SiN layers, rotated by an angle θ relative to the illumination injection plane.

Optics EXPRESS

Finally, varying the propagation angle affects the composite nonlinearity, expressed through the coefficient ζd defined in Eq. (7). Changes in θ affect this coefficient through the modified polarization of the interacting waves relative to the intrinsic GaAs axes. In addition, the field distributions used in Eq. (8) are themselves angle dependent [37]. Figure 3(C) shows the effective nonlinearities extracted by fitting Eq. (7) to the simulated intensities. For the parameters studied here, the fitted data closely follows the curve $\zeta_0 d_0 \cos(\theta)$, obtained assuming that the angular dependence arises only from changes in the orientation relative to the GaAs axes. Here, $\zeta_0 d_0$ is the coefficient at parallel propagation, calculated using Eq. (8).

All-together, this shows that the bulk metamaterial approach can be used for both structural and angular tunable SHG, even by using isotropic building blocks, that do not support BPM in their natural form.

3.2. Difference frequency generation

To explore the potential of angle tuned FBPM metamaterials for additional applications, we studied also DFG in the composite structure. DFG in nonlinear crystals has been central to the development of coherent mid-IR sources, with applications that include spectroscopy, medical diagnostics, medical procedures, and material processing [45]. Therefore, we focused on the potential for efficient generation of mid-IR radiation by the metamaterial.

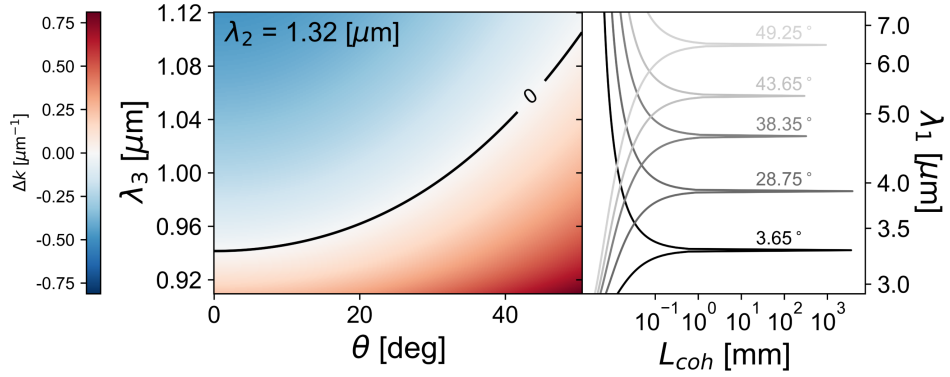

Fig. 4. Angle tuned mid-IR generation with d_{GaAs} = 120 nm and d_{SiN} = 12 nm. Left - momentum mismatch map for DFG with one fixed wavelength λ_2 = 1.32 μm, and one tunable wavelength ~ 0.91<λ_3<1.12 μm. Varying the angle in the range 0° – 50° allows PM of DFG over a full octave, as can be seen on the right, where the coherence lengths are shown for selected angles.

Using the convention $\lambda_1 > \lambda_2 > \lambda_3$ for the free-space wavelengths of the three interacting waves, the momentum mismatch of a DFG process is

$$\Delta k = 2\pi \left(\frac{n_{\lambda_3}}{\lambda_3} - \frac{n_{\lambda_2}}{\lambda_2} - \frac{n_{\lambda_1}}{\lambda_1} \right) \tag{9}$$

where $\lambda_1 = \frac{\lambda_2 \lambda_3}{\lambda_2 - \lambda_3}$ is the output wavelength. For our calculations we considered DFG between a tunable TM polarized wave λ_3 that is swept in the range ~ 0.91 – 1.12 μm, and a fixed TE polarized wave with λ_2 = 1.32 μm. This wavelength combination was selected in order to allow for comparison with existing form-birefringence DFG tunability data [26]. Keeping the nonlinear film thickness d_{GaAs} = 120 nm, a suitable SiN thickness is found to be ~ 10 nm. Figure 4 displays the momentum mismatch map of the described process. By varying the propagation angle between 0°<θ<50° and examining a TE polarized difference frequency signal, the PM

Optics EXPRESS

condition can be tuned to support generation of light over a full octave in the Mid-IR, between $\sim 3.3 - 6.7\ \mu m$. The PM bandwidth in this example is limited by absorption in SiN, which starts being pronounced around 6.7 μm [40]. Comparing this result with temperature tuning in form-birefringent waveguide systems which used similar illumination wavelengths, a $\sim 100°C$ shift in temperature allowed tuning λ_1 in a bandwidth of $\sim 0.4\ \mu m$ between $5.2 - 5.6\ \mu m$ [26]. The frequency bandwidth calculated here with the bulk metamaterial is more than 10 times larger. Since the field distributions in the layers are not expected to change substantially, we anticipate that the dependence of the nonlinearity on propagation angle will be similar to that shown in Fig. 3(C).

4. Conclusions and discussion

To conclude, we have studied FBPM in bulk laminar composites as a promising metamaterial platform for tunable PM of frequency conversion processes. Focusing on the combination of GaAs and SiN, we analyzed the PM conditions for SHG under propagation parallel to the metamaterial layers to show the dependence of the PM frequency on the layer thickness. We then used overlap analysis of the interacting waves to calculate the composite effective nonlinear coefficients for several SiN thickness values. Our calculations closely match simulation results, allowing for a comprehensive model for designing the metamaterials. We have further shown that by using the propagation angle degree of freedom, highly tunable frequency converters can be designed. In addition to SHG, we focused on the application to generation of mid-IR radiation, and have shown that angle tuning in the studied FBPM metamaterial potentially enables efficient mid-IR generation in a bandwidth window of over an octave. This range is 10 times broader than that demonstrated in similar form-birefringent waveguide systems [26].

From the data presented in Fig. 3(C), the nonlinear figure of merit (FOM), defined as $(\zeta d)^2/n^3$ (n is the average effective index), can be calculated. For the parameters analyzed, the FOM at a propagation angle of 0° is approximately 107% compared to the value of orientation-patterned GaAs (OP-GaAs) devices [38,46]. At a propagation angle of 50°, it decreases to about 45% relative to OP-GaAs. Thus, the form-birefringent geometry offers an angle-tunable nonlinear platform whose FOM is predicted to exceed or be comparable to most birefringent mid-IR nonlinear crystals [47], while enabling engineered spectral properties and functionalities, similar to those supported today by domain inversion techniques and integrated nonlinear devices [48,49].

The practical realization of an angle tunable component as described here requires fabricating a macro scale metamaterial, with each period being considerably-subwavelength. Growing crystalline GaAs layers together with amorphous SiN layers may pose significant challenges. One possible route to overcome this difficulty is through techniques of heterogeneous integration. Such techniques, among various achievements are used for incorporation of III-V materials with SiN through micro-transfer and wafer bonding methods [50,51]. Specifically, integration of GaAs devices using few nm SiN layers has been experimentally demonstrated [48,49]. Although current fabrication schemes applied directly to the described metamaterial might be prohibitively time-consuming, this may not necessarily represent an intrinsic limitation. We therefore regard these ongoing technological developments as promising pathways towards fabricating the proposed device.

Another important point to consider is that any fabrication method will inevitably introduce inhomogeneities into the system which need to be taken into account. For example, SiN films with thicknesses of 10-20 nm are reported to have uniformity of 4-5% [52,53]. In the specific case shown in Fig. 2(A), for a film with a nominal thickness of 20 nm, a 4% variation can lead up to an $\sim \pm 8$ nm shift in the PM wavelength. However, this will be the case only if the variation will be uniform across all the layers and the interaction volume. Since non-uniformity would be distributed across the beam waist as well as along the propagation length, its effects may lead to an inhomogeneous broadening of the PM curve around the calculated values.

Optics EXPRESS

Finally, methods to construct various types of 3D nonlinear metamaterials and heterostructures are in constant progress [13,30,31,34,35]. For example recently, techniques enabling deep-subwavelength patterning of bulk transparent materials, including LiNbO3 have been reported [34]. Although we have used a particular material combination and specific frequency bands in our calculations, our results can be applied to other combinations of transparent isotropic materials and frequencies under which the assumptions of the model described above are met. They can also, with some care, be generalized to involve birefringent layers, to increase or diminish the natural birefringence.

In view of the potential benefits of form birefringent nonlinear metamaterials, along with recent technological advancements and research efforts, we believe that the concept of bulky laminar nonlinear metamaterials, more than few-layer thick, may be feasible in the foreseeable future and will open new avenues for nonlinear optics.

Funding. European Research Council (ERC 3D NOAM 101044797).

Acknowledgments. M.T. acknowledges the support by the Milner Foundation fellowship for PhD students.

Disclosures. The authors declare no conflicts of interest.

Data availability. Data underlying the results presented in this paper are not publicly available at this time but may be obtained from the authors upon reasonable request.

References

1. I. Breunig, D. Haertle, and K. Buse, "Continuous-wave optical parametric oscillators: recent developments and prospects," Appl. Phys. B **105**(1), 99–111 (2011).
2. L. E. Myers and W. R. Bosenberg, "Periodically poled lithium niobate and quasi-phase-matched optical parametric oscillators," IEEE J. Quantum Electron. **33**(10), 1663–1672 (1997).
3. P. S. Kuo, V. B. Verma, and S. W. Nam, "Demonstration of a polarization-entangled photon-pair source based on phase-modulated PPLN," OSA Continuum **3**(2), 295–304 (2020).
4. T. Santiago-Cruz, S. D. Gennaro, O. Mitrofanov, *et al.*, "Resonant metasurfaces for generating complex quantum states," Science **377**(6609), 991–995 (2022).
5. N. Bloembergen, "Wave propagation in nonlinear electromagnetic media," Proc. IEEE **51**(1), 124–131 (1963).
6. K. Moutzouris, S. Venugopal Rao, M. Ebrahimzadeh, *et al.*, "Second-harmonic generation through optimized modal phase matching in semiconductor waveguides," Appl. Phys. Lett. **83**(4), 620–622 (2003).
7. C. Wang, X. Xiong, N. Andrade, *et al.*, "Second harmonic generation in nano-structured thin-film lithium niobate waveguides," Opt. Express **25**(6), 6963–6973 (2017).
8. M. M. Fejer, G. Magel, D. H. Jundt, *et al.*, "Quasi-phase-matched second harmonic generation: tuning and tolerances," IEEE J. Quantum Electron. **28**(11), 2631–2654 (1992).
9. G. Boyd, R. C. Miller, K. Nassau, *et al.*, "LiNbO3: an efficient phase matchable nonlinear optical material," Appl. Phys. Lett. **5**(11), 234–236 (1964).
10. A.-Y. Zhou, W.-L. Zhang, C.-S. Lin, *et al.*, "Ba10In6Zn7S26-n ZnS: An Inorganic Composite System with Interface Phase-Matching Tuned for High-Performance Infrared Nonlinear Optical Materials," Inorg. Chem. **58**(6), 3990–3999 (2019).
11. A. Yariv and P. Yeh, "Electromagnetic propagation in periodic stratified media. II. Birefringence, phase matching, and x-ray lasers," J. Opt. Soc. Am. **67**(4), 438–447 (1977).
12. N. Bloembergen and A. Sievers, "Nonlinear optical properties of periodic laminar structures," Appl. Phys. Lett. **17**(11), 483–486 (1970).
13. V. Novikov, A. Maydykovskiy, B. Mantsyzov, *et al.*, "Laue diffraction in one-dimensional photonic crystals: The way for phase-matched second-harmonic generation," Phys. Rev. B **93**(23), 235420 (2016).
14. C. Duncan, L. Perret, S. Palomba, *et al.*, "New avenues for phase matching in nonlinear hyperbolic metamaterials," Sci. Rep. **5**(1), 8983 (2015).
15. L. Brekhovskikh, *Waves in layered media* (Elsevier, 2012), vol. 16, chap. 1.7.
16. J. Van der Ziel, "Phase- matched harmonic generation in a laminar structure with wave propagation in the plane of the layers," Appl. Phys. Lett. **26**(2), 60–61 (1975).
17. A. Yariv and P. Yeh, *Optical waves in crystal propagation and control of laser radiation* (John Wiley and Sons, Inc., 1983).
18. B. Desiatov, N. Mazurski, Y. Fainman, *et al.*, "Polarization selective beam shaping using nanoscale dielectric metasurfaces," Opt. Express **23**(17), 22611–22618 (2015).
19. Y. Yermakov, A. I. Ovcharenko, A. A. Bogdanov, *et al.*, "Spin control of light with hyperbolic metasurfaces," Phys. Rev. B **94**(7), 075446 (2016).
20. N. A. Rubin, A. Zaidi, A. H. Dorrah, *et al.*, "Jones matrix holography with metasurfaces," Sci. Adv. **7**(33), eabg7488 (2021).

Optics EXPRESS

21. S. L. Neale, M. P. MacDonald, K. Dholakia, *et al.*, "All-optical control of microfluidic components using form birefringence," Nat. Mater. **4**(7), 530–533 (2005).
22. D. Andrén, D. G. Baranov, S. Jones, *et al.*, "Microscopic metavehicles powered and steered by embedded optical metasurfaces," Nat. Nanotechnol. **16**(9), 970–974 (2021).
23. J. M. Luque-González, A. Sánchez-Postigo, A. Hadij-ElHouati, *et al.*, "A review of silicon subwavelength gratings: building break-through devices with anisotropic metamaterials," Nanophotonics **10**(11), 2765–2797 (2021).
24. A. Fiore, V. Berger, E. Rosencher, *et al.*, "Phase matching using an isotropic nonlinear optical material," Nature **391**(6666), 463–466 (1998).
25. A. Fiore, S. Janz, L. Delobel, *et al.*, "Second-harmonic generation at λ= 1.6 μm in AlGaAs/Al2O3 waveguides using birefringence phase matching," Appl. Phys. Lett. **72**(23), 2942–2944 (1998).
26. P. Bravetti, A. Fiore, V. Berger, *et al.*, "5.2-5.6-μm source tunable by frequency conversion in a GaAs-based waveguide," Opt. Lett. **23**(5), 331–333 (1998).
27. C. Ozanam, M. Savanier, L. Lanco, *et al.*, "Toward an AlGaAs/AlOx near-infrared integrated optical parametric oscillator," J. Opt. Soc. Am. B **31**(3), 542–550 (2014).
28. A. De Rossi, V. Berger, G. Leo, *et al.*, "Form birefringence phase matching in multilayer semiconductor waveguides: tuning and tolerances," IEEE J. Quantum Electron. **41**(10), 1293–1302 (2005).
29. N. A. Otman and M. Čada, "Phase-matched mid-infrared difference frequency generation using a nanostructured gallium arsenide metamaterial with nanoholes," IEEE Photonics J. **12**(3), 1–10 (2020).
30. G. Marino, D. Rocco, C. Gigli, *et al.*, "Harmonic generation with multi-layer dielectric metasurfaces," Nanophotonics **10**(7), 1837–1843 (2021).
31. T. Stolt, J. Kim, S. Héron, *et al.*, "Backward phase-matched second-harmonic generation from stacked metasurfaces," Phys. Rev. Lett. **126**(3), 033901 (2021).
32. D. Ben-Haim and T. Ellenbogen, "Optical Anomalies due to Volume Collective Modes of Plasmonic Metamaterials," Laser Photonics Rev. **17**(4), 2200671 (2023).
33. G. Roberts, C. Ballew, T. Zheng, *et al.*, "3D-patterned inverse-designed mid-infrared metaoptics," Nat. Commun. **14**(1), 2768 (2023).
34. Z.-Z. Li, H. Fan, L. Wang, *et al.*, "Super-stealth dicing of transparent solids with nanometric precision," Nat. Photonics **18**(8), 799–808 (2024).
35. E. Gribaudo, M. Deckart, P. Vlugter, *et al.*, "Sub-wavelength femtosecond laser based nanostructuring of complex patterns in the bulk of fused silica," Opt. Express **33**(5), 11529–11540 (2025).
36. C. Gu and P. Yeh, "Form birefringence dispersion in periodic layered media," Opt. Lett. **21**(7), 504–506 (1996).
37. P. Yeh, A. Yariv, and C.-S. Hong, "Electromagnetic propagation in periodic stratified media. I. General theory," J. Opt. Soc. Am. **67**(4), 423–438 (1977).
38. T. Skauli, K. Vodopyanov, T. Pinguet, *et al.*, "Measurement of the nonlinear coefficient of orientation-patterned GaAs and demonstration of highly efficient second-harmonic generation," Opt. Lett. **27**(8), 628–630 (2002).
39. S. Hayashi, D. Bruno, R. Sandhu, *et al.*, "Wafer bonding for III-V on insulator structures," J. Electron. Mater. **32**(8), 877–881 (2003).
40. R. Soref, "Mid-infrared photonics in silicon and germanium," Nat. Photonics **4**(8), 495–497 (2010).
41. T. Skauli, P. Kuo, K. Vodopyanov, *et al.*, "Improved dispersion relations for GaAs and applications to nonlinear optics," J. Appl. Phys. **94**(10), 6447–6455 (2003).
42. A. Yariv, "Coupled-mode theory for guided-wave optics," IEEE J. Quantum Electron. **9**(9), 919–933 (1973).
43. R. Regener and W. Sohler, "Efficient second-harmonic generation in Ti:LiNbO3 channel waveguide resonators," J. Opt. Soc. Am. B **5**(2), 267–277 (1988).
44. COMSOL, "Second Harmonic Generation in the Frequency Domain," Accessed on March 24th, 2024.
45. H. Pires, M. Baudisch, D. Sanchez, *et al.*, "Ultrashort pulse generation in the mid-IR," Prog. Quantum Electron. **43**, 1–30 (2015).
46. Q. Fu, L. Xu, S. Liang, *et al.*, "High-average-power picosecond mid-infrared OP-GaAs OPO," Opt. Express **28**(4), 5741–5748 (2020).
47. P. G. Schunemann, K. T. Zawilski, L. A. Pomeranz, *et al.*, "Advances in nonlinear optical crystals for mid-infrared coherent sources," J. Opt. Soc. Am. B **33**(11), D36–D43 (2016).
48. L. Chang, A. Boes, X. Guo, *et al.*, "Heterogeneously integrated GaAs waveguides on insulator for efficient frequency conversion," Laser Photonics Rev. **12**(10), 1800149 (2018).
49. L. Chang, A. Boes, P. Pintus, *et al.*, "Strong frequency conversion in heterogeneously integrated GaAs resonators," APL Photonics **4**(3), 036103 (2019).
50. G. Roelkens, J. Zhang, L. Bogaert, *et al.*, "Micro-transfer printing for heterogeneous Si photonic integrated circuits," IEEE J. Sel. Top. Quantum Electron. **29**(3: Photon. Elec. Co-Inte. and Ad), 1–14 (2023).
51. M. A. Tran, C. Zhang, T. J. Morin, *et al.*, "Extending the spectrum of fully integrated photonics to submicrometre wavelengths," Nature **610**(7930), 54–60 (2022).
52. D. Park, M. Tao, D. Li, *et al.*, "Gate quality Si3N4 prepared by low temperature remote plasma enhanced chemical vapor deposition for III-V semiconductor-based metal-insulator-semiconductor devices," J. Vac. Sci. & Technol. B: Microelectron. Nanometer Struct. Process. Meas. Phenom. **14**(4), 2674–2683 (1996).
53. Norcada, "Technical Information Page," Accessed on October 23rd, 2024.